

Convection in binary mixtures: the role of the concentration field

M. Lücke^a, W. Barten^a and M. Kamps^b

^a*Institut für Theoretische Physik, Universität des Saarlandes, W-6600 Saarbrücken, Germany*

^b*Stabsstelle Supercomputing, Forschungszentrum, W-5170 Jülich, Germany*

Structure and dynamics of different roll states appearing close to onset of convection in binary mixtures and the influence of the concentration field on the properties of these states are elucidated. Numerical solutions of the hydrodynamic field equations in a vertical cross section perpendicular to the roll axes are reviewed for room temperature ethanol–water parameters. Extended states of stationary overturning convection (SOC) and of traveling wave (TW) convective rolls are investigated as well as spatially confined states of localized traveling wave (LTW) rolls. The field structure and symmetries of these states are discussed. The appearance of a concentration contrast in TW's between rolls of different turning sense is explained. A mean lateral concentration current that is generated in the TW state by the phase difference between the concentration wave and the velocity wave is reviewed. A comparison of LTW's of arbitrary and selected width obtained for different fluid parameters reveals the same field structure under the leading and trailing fronts of these states with only the extensions of the center parts being different. The presence of a large-scale concentration current, the associated large-scale concentration redistribution, and the resulting hindering of the drift of the LTW is reviewed.

1. Introduction

Convection in horizontal layers of binary fluid mixtures^{#1}, such as ethanol–water, heated from below has been investigated quite intensively, both experimentally [2–27] as well as theoretically [28–52]. This thermally driven system is experimentally and theoretically very well suited to study a variety of different linear and nonlinear pattern forming phenomena in dissipative continuous systems. Note that as a result of the additional degrees of freedom of the concentration field being coupled via the Soret effect to the temperature field convective patterns in mixtures appear in the vicinity of the primary instabilities of the laterally homogeneous basic state of conduction in a dynamically and struc-

turally much richer variety than for standard Rayleigh–Bénard convection in a pure fluid.

Here we focus our attention on mixtures with negative Soret coupling, $\psi < 0$. Then, upon increasing the Rayleigh number r the first instability occurs at a Hopf bifurcation threshold, r_{osc} , while the threshold for growth of stationary convection is often at much larger thermal driving, $r_{stat} > r_{osc}$. At r_{osc} a TW solution of propagating convective rolls branches off the quiescent conductive state. For a wide parameter region this bifurcation is backwards into an unstable TW branch which bends upwards and connects via a saddle node to an upper branch. This upper branch locates stable, nonlinear TW states. Eventually the TW branch ends with zero frequency by merging into the SOC solution branch of stationary states that has subcritically bifurcated at r_{stat} . This knowledge of the bifurcation structure has grown over the years since the first observation of TW's in rectangular cells [2–5] by

^{#1}For an early review see ref. [1]. For later work we refer to the references in recent experimental [2–27] and theoretical [28–52] papers.

accumulating various bits of information coming from experiments, amplitude equations [28,29], Galerkin models [30–32], numerical solutions of the full field equations [33–37], and analytical approaches using boundary layer techniques [38]. Moreover, recent experiments in annular cells showed quantitative agreement [6] with the analytical [38] and numerical [36] bifurcation behaviour. Also the field structure of the TW and SOC states including the boundary layer properties of the concentration field has now been elucidated numerically in quantitative detail [34,36]^{#2}. The results of these calculations for top view shadowgraph intensity profiles compare quite well with measurements of the latter [7]. Hence using the numerical information it was possible to distinguish and study the concentration field also experimentally as a function of r , e.g., when approaching the TW \leftrightarrow SOC transition [7]. Most recently the concentration field of TW states was extracted quantitatively [8] from experimental side view shadowgraphs by using fits to the laterally trapezoidal form of the numerically obtained [34,36] TW concentration profiles. The latter reflect a concentration contrast between TW rolls which breaks the mirror symmetry between left and right turning rolls and which decreases when approaching the transition TW \rightarrow SOC.

In addition to and competing with the stable, nonlinear extended TW or SOC there are stable LTW states – their occupation depends, e.g., on initial conditions. LTW's consist of traveling convective rolls that are spatially confined under a pulse-like intensity envelope which drops via two fronts to zero into the surrounding quiescent conductive state. First being observed [4,9] in rectangular cells near a sidewall, their existence was related [39] to lossy wall reflection and the convective nature of the instability. However, the subsequent experiments in annular cells producing LTW's with various widths below onset at

$\psi \approx -0.25$ [10] and with uniquely selected width below and above onset at $\psi \approx -0.1$ [11,12] showed the intrinsic nature of LTW states. Furthermore, LTW's in rectangular and annular cells were shown to be similar [11] and the former were also found [13,14] sitting in the cell center, away from the walls. Subcritical LTW's with various widths and a supercritical LTW state with selected width were also generated by numerical integration of the full hydrodynamic field equations for experimental parameters [40]^{#3}. An analysis of their structure [40] shows their similarity (cf. section 4). We also mention that comparing experimental top view shadowgraph measurements with shadowgraph intensities from the simulations [40] quantitative agreement was found for LTW's of various widths [15] and for LTW states of selected width [16].

Subcritical pulse solutions of selected width were also found in complex Ginzburg–Landau equations with quintic amplitude terms [41,42]. However, these pulses being packets of linear waves moved with the large group velocity of the latter whereas the early experimental LTW's [4,9–12,14,15,17–19] were motionless after transients. While adding [43] cubic nonlinear gradient terms to the Ginzburg–Landau equation can change the pulse velocity and shape, numerical simulations of the full field equations suggest that a large-scale current-induced concentration redistribution hinders the pulse motion and reduces the drift velocity of LTW's to very small values [40]. Such small group velocities v_g in the direction of roll propagation have then also been found in cells with improved homogeneity [16,20]. The experimental observation [16,20] that v_g decreases (and eventually may even change sign [16]) when the LTW

^{#2}In this paper the correct ordinate labels of fig. 5a are $U(10^{-2}\kappa/d)$ and $\varphi_w(10^{-3} \times 2\pi)$.

^{#3}The wavelength $\lambda(x)$ in figs. 2a and 4a of [40] is defined via node distances. This definition is not strictly local. It magnifies structural variations of small amplitude fields behind the trailing edge. Thus the strong increase of λ there is misleading.

frequency grows with decreasing r is discussed in section 4.3 in terms of an associated increase of the concentration redistribution.

In this work we discuss the influence of the concentration field and some of the phenomena intimately related to it in extended TW and SOC states and in LTW states. In section 2 we describe the system and our numerical method to investigate it. In section 3 the bifurcation properties of TW and SOC are reviewed and a detailed comparison of their structural properties is given. We explain the mirror symmetry breaking appearance of a concentration contrast in TW's and we review phase-induced mean lateral currents. Section 4 deals with LTW states. We compare LTW's of selected and arbitrary width and we discuss the interplay between the structural dynamics of LTW's, the large-scale current in the latter, the large-scale field modifications, and the behaviour of the drift velocity. Section 5 contains concluding remarks on the role of the concentration field in convection in mixtures.

2. The system

Consider a horizontal fluid layer of, say, an alcohol water mixture heated from below between two plates that are good heat conductors and thereby impose a laterally homogeneous temperature boundary condition. The mixture is characterized by two time-scale ratios: The Prandtl number $\sigma = \nu/\kappa$ is the kinematic viscosity ν , i.e., the momentum diffusivity, divided by the heat diffusivity κ . In ethanol water mixtures considered here σ is about 10. The Lewis number $L = D/\kappa$ is the alcohol concentration diffusion constant D divided by κ . Since concentration diffusion in the mixture is about 100 times slower than heat diffusion, the relaxation times that have to be waited out in experiments as well as in numerical simulations are about 100 times longer than in pure water. On the one hand that is inconvenient, but on the other hand it is the

concentration field that causes a wealth of new convection phenomena in mixtures.

2.1. The equations

The balance equations of mass, momentum, heat, and concentration read in Oberbeck Bousinesq approximation

$$\nabla \cdot \mathbf{u} = 0, \quad (2.1a)$$

$$(\partial_t + \mathbf{u} \cdot \nabla) \mathbf{u} = -\nabla p + \sigma \nabla^2 \mathbf{u} + b \mathbf{e}_z, \quad (2.1b)$$

$$(\partial_t + \mathbf{u} \cdot \nabla) T = \nabla^2 T, \quad (2.1c)$$

$$(\partial_t + \mathbf{u} \cdot \nabla) C = L \nabla^2 (C - \psi T). \quad (2.1d)$$

Here \mathbf{u} is the velocity field. The deviations $\delta F = F - F_0$ of the pressure p , the temperature T , and the concentration C from their respective mean values F_0 are small. Then the vertical buoyancy force density is

$$b = \sigma R (\delta T + \delta C). \quad (2.2)$$

The Rayleigh number is

$$R = \frac{\alpha g d^3}{\kappa \nu} \Delta T \quad (2.3)$$

and the separation ratio

$$\psi = -\frac{\beta}{\alpha} \frac{k_T}{T_0} \quad (2.4)$$

with g the gravitational constant, d the layer thickness, ΔT the vertical temperature difference across the layer, $\alpha = -(1/\rho) \partial \rho(T, p, C) / \partial T$ the thermal expansion coefficient, $\beta = -(1/\rho) \partial \rho(T, p, C) / \partial C$ the solutal expansion coefficient, and k_T the thermodiffusion ratio of the mixture. We measure lengths in units of d , times by the vertical thermal diffusion time d^2/κ , temperature by ΔT , and concentration by $\Delta T \alpha / \beta$.

The concentration is changed convectively by the velocity field and furthermore via the Soret effect by the temperature field. The latter effect implies that temperature differences contribute to the concentration current

$$\mathbf{J} = \mathbf{u} \delta C - L \nabla(C - \psi T). \quad (2.5)$$

In states like the quiescent basic conductive state

$$\begin{aligned} \mathbf{u}_{\text{cond}} &= 0, \quad \delta T_{\text{cond}} = \frac{1}{2} - z, \\ \delta C_{\text{cond}} &= \psi(\frac{1}{2} - z), \end{aligned} \quad (2.6)$$

where $\mathbf{J} = 0$ the Soret effect generates a temperature induced concentration gradient. Thus $\psi = \delta C_{\text{cond}} / \delta T_{\text{cond}}$ measures the strength of the Soret effect. It can be positive or negative and thus either enhances or depresses the buoyancy

$$b_{\text{cond}} = \sigma R(\frac{1}{2} - z)(1 + \psi). \quad (2.7)$$

Here the layer extends vertically from $z = 0$ to $z = 1$. Without Soret effect, $\psi = 0$, the concentration δC relaxes to zero so that $\psi = 0$ is hydrodynamically equivalent to a pure fluid.

While the pure fluid is characterized by two parameters, σ and R , in the mixture we have in addition L and ψ . Conventionally the two material parameters σ and L are considered to be fixed, while R measuring the thermal part of the buoyancy force (2.7) and ψ the strength of the Soret coupling are taken as control parameters. In the following we shall use instead of R the reduced Rayleigh number

$$r = R/R_c(\psi = 0), \quad (2.8)$$

with $R_c(\psi = 0)$ being the critical one for onset of convection in a pure fluid. We also introduce the convective parts

$$c = C - C_{\text{cond}}, \quad \theta = T - T_{\text{cond}} \quad (2.9)$$

of the concentration and temperature fields.

2.2. Numerical simulation

We have numerically solved the field equations (2.1) in a vertical x - z section of the layer perpendicular to the axes of the convective rolls by suppressing any y -dependence of the fields. Thus the velocity field

$$\mathbf{u} = u(x, z; t) \mathbf{e}_x + w(x, z; t) \mathbf{e}_z \quad (2.10)$$

has a lateral component u and a vertical component w . The horizontal boundaries are rigid, isothermal, and impermeable. Lateral boundaries are periodic, $F(x, z; t) = F(x + \Gamma, z; t)$. To simulate extended states we took $\Gamma = 2$ corresponding to a wave number $k = \pi$ very close to the critical one [34,36]. Stable LTW states were found for $\Gamma = 20$ and 40 to coexist with stable extended TW or SOC states [40]. Whether an LTW state or an extended state evolves depends on the history of the system.

We used the MAC method [53] to discretize the fields with uniform spatial resolution $\Delta x = \Delta z = 0.05$. Spatial derivatives are replaced by central differences and for time differences we use a forward Euler step. Pressure and velocity fields are iteratively adapted [54] to each other. All simulations presented here were done for $L = 0.01$ and $\sigma = 10$. Then typical relaxation times towards an SOC, TW, LTW state were about 5, 100, 500 vertical thermal diffusion times, respectively.

3. Extended states: stationary and traveling convective rolls

In this section we review characteristic convection properties of extended SOC and TW states occurring at negative separation ratios.

3.1. Bifurcation structure

In a pure fluid ($\psi = 0$) a stable, spatially periodic SOC state of parallel rolls branches off the

conductive state when increasing the thermal stress beyond the convective threshold $r_{\text{stat}}(\psi = 0) = 1$ as shown by the dotted line in fig. 1b. The transition to convection is second order in the language of Landau's mean field classification of equilibrium phase transitions with the order parameter, the deviation of the Nusselt number from 1, initially increasing linearly. Upon decreasing ψ the bifurcation threshold $r_{\text{stat}}(\psi)$ moves to larger r while the bifurcated SOC branch rapidly approaches the dotted $\psi = 0$ line. Thus the initial slope of the Nusselt number steepens up. With further decreasing ψ the SOC order parameter goes through a tricritical point

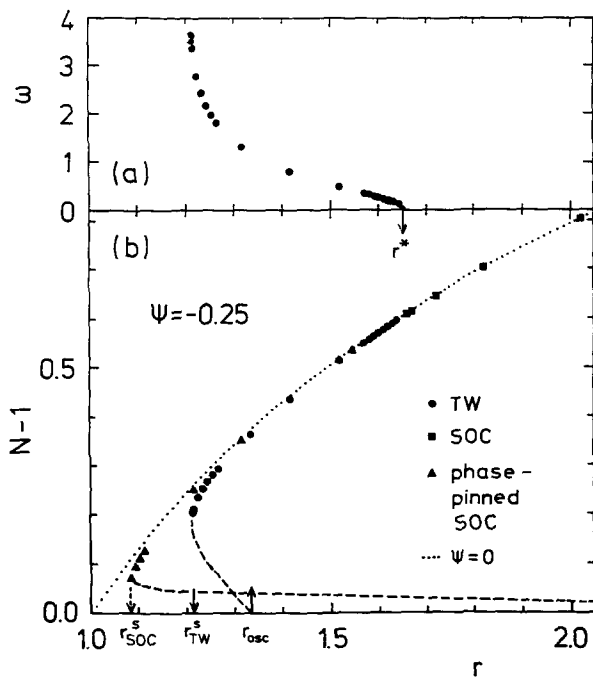


Fig. 1. Numerically obtained bifurcation properties of nonlinear convective states. a) Frequency of stable TW and b) Nusselt numbers vs r . Full dots and squares (thin dots) refer to states in the mixture (pure fluid) that are stable under lateral periodic boundary conditions. At r^* the TW branch merges nonhysteretically with zero frequency with the SOC branch. Full triangles denote SOC states in the mixture that have been stabilized by phase pinning lateral boundaries. We identify the lowest TW (SOC) state with the saddle $r_{\text{TW}}^s(r_{\text{SOC}}^s)$ of the TW (SOC) solution branch. Dashed lines denoting unstable bifurcation branches are schematic. $\psi = -0.25$, $r_{\text{osc}}(k = \pi) = 1.3347$ [45], $\omega_{\text{H}}(k = \pi) = 11.235$ [45], $r_{\text{TW}}^s = 1.215$, $r_{\text{SOC}}^s = 1.08$, $r^* \approx 1.65$.

[29] with infinite initial slope beyond which the transition becomes first order. The SOC branch forms a saddle relatively close to the $\psi = 0$ line while the bifurcation threshold, $r_{\text{stat}}(\psi)$, moves to ever larger r . Such a situation is shown in fig. 1b.

For sufficiently negative ψ there is also a Hopf bifurcation threshold, r_{osc} [29,44,45]. There a solution describing TW convective rolls branches off the conductive state. First the TW bifurcation is forwards. However, seeing such a forwards bifurcation in ethanol-water is difficult. There are some hints in ^3He - ^4He mixtures [21]. Then, with decreasing ψ the initial slope of the TW Nusselt number steepens up, there is a tricritical TW transition [29], and beyond that it is a hysteretic backwards bifurcation as shown in fig. 1b. The reason for the associated discontinuous onset of convection is a nonlinear feedback [47]: For $\psi < 0$ the Soret induced conductive concentration distribution weakens the buoyancy. Convection, on the other hand, redistributes the alcohol more evenly thereby reducing the adverse Soret effect and thus increasing the buoyancy. The increased buoyancy in turn strengthens convection which again amplifies the buoyancy.

Moving along the TW solution branch the frequency decreases monotonously from the Hopf value ω_{H} at the bifurcation point r_{osc} to zero at r^* as shown in fig. 1a. At the saddle node where TW convection first becomes stable ω has dropped already to about $\omega_{\text{H}}/3$ for $\psi = -0.25$. At r^* there is under laterally periodic boundary conditions a nonhysteretic transition [6,36,38] to SOC. There the frequency vanishes $\sim \sqrt{r^* - r}$. The r variation of ω shown in fig. 1a agrees after appropriate rescaling [6] very well with recent experiments [6] and theoretical results [38]. With increasing ψ the zero-frequency endpoint r^* of the TW branch glides along the SOC branch towards the SOC saddle, and then onto the lower SOC branch where it moves away from the saddle.

The SOC states marked by full triangles in fig.

1b below the TW endpoint at r^* are unstable. Thus stable SOC and stable TW states do not coexist there. By pinning the phase of the hydrodynamic fields we have suppressed the TW states and thereby stabilized these SOC states in fig. 1b. Releasing the phase pinning the SOC convective rolls evolve for $r_{TW}^s < r < r^*$ into a TW and for $r_{SOC}^s < r < r_{TW}^s$ they decay into the conductive state. The upper unstable SOC branch can also be stabilized in experiments [22].

3.2. Comparison of TW and SOC states

The vertical convective heat transport of the TW rapidly approaches that one of SOC which in turn is close to the one in the corresponding pure fluid. So one expects the temperature and velocity field structure of these states to be somewhat similar which is indeed the case [36,7]. But the concentration field in TW rolls differs significantly from that one in SOC rolls as demonstrated in fig. 2. There we show in the left plate a right propagating TW close to the saddle and in the right plate an SOC state slightly above r^* . In (a) we display lateral profiles of the vertical velocity field w , of δC , and of δT at midheight, $z = \frac{1}{2}$, of the fluid layer. In (b)–(e) we show in x – z sections of the layer the velocity field, the alcohol concentration, streamlines of the velocity field in a frame that for the TW is comoving with the phase velocity of the TW, and finally the side view shadowgraph intensity distribution [23]

$$I(x, z) = (\partial_x^2 + \partial_z^2)(C + aT) \quad (3.1)$$

that one would see by shining light parallel to the roll axes through the layer. Here $a = -0.919$ [7]. In fact the experimental shadowgraph pictures of Winkler and Kolodner [8] of TW and SOC states look in remarkable detail similar to those in (e) following from our numerical simulation [36]. SOC as well as TW states have a glide-mirror symmetry [34]

$$\delta F(x, z; t) = \pm \delta F(x + \frac{1}{2}\lambda, 1 - z; t) \quad (3.2)$$

around the mid-layer plane $z = \frac{1}{2}$ with + for u , p and – for w , T , C . This symmetry is most easily seen in fig. 2e.

If one moves along the upper TW branch from the saddle at r_{TW}^s to the TW end point r^* and beyond it onto the SOC branch by increasing the thermal stress the concentration field shows the most conspicuous changes. Those of u and T are much smaller but can be seen in a lateral Fourier analysis. Furthermore, the concentration field in fig. 2 most clearly reveals that both states are strongly nonlinear in the sense that their lateral variation differs significantly from the critical one, $e^{ik_c x}$.

In the SOC state the fields of left and right turning rolls are mirror symmetric to each other and thus also the alcohol distribution displays this symmetry. As an aside we mention that we could get the unstable SOC states on the upper branch also by using a symmetry conserving property [55] of our numerical code. In the SOC state the layer is well mixed convectively as demonstrated by the predominance of the green colour for $C \approx C_0$ in the bulk of the layer in fig. 2c right plate. There are small concentration variations in the upflow (yellow vertical stripe) and downflow (blue vertical stripe) regions between the rolls and more intense concentration variations in the narrow boundary layers of alcohol rich (blue) and alcohol poor (red) fluid near the top and bottom plates. But convection has greatly reduced the Soret induced vertical concentration difference between top and bottom [34].

The mirror symmetry of SOC between left and right turning rolls is broken to a varying degree in all fields upon *decreasing* the driving r below r^* in the transition to the TW state that is stable at lower driving. With decreasing r and increasing ω the TW state develops a monotonously increasing concentration contrast [34,36]: in a right propagating TW the right (left) turning rolls are alcohol rich (poor) as shown by the blue (yellow) colours in the left plate of fig. 2. Simultaneously the widths of the boundary layers at

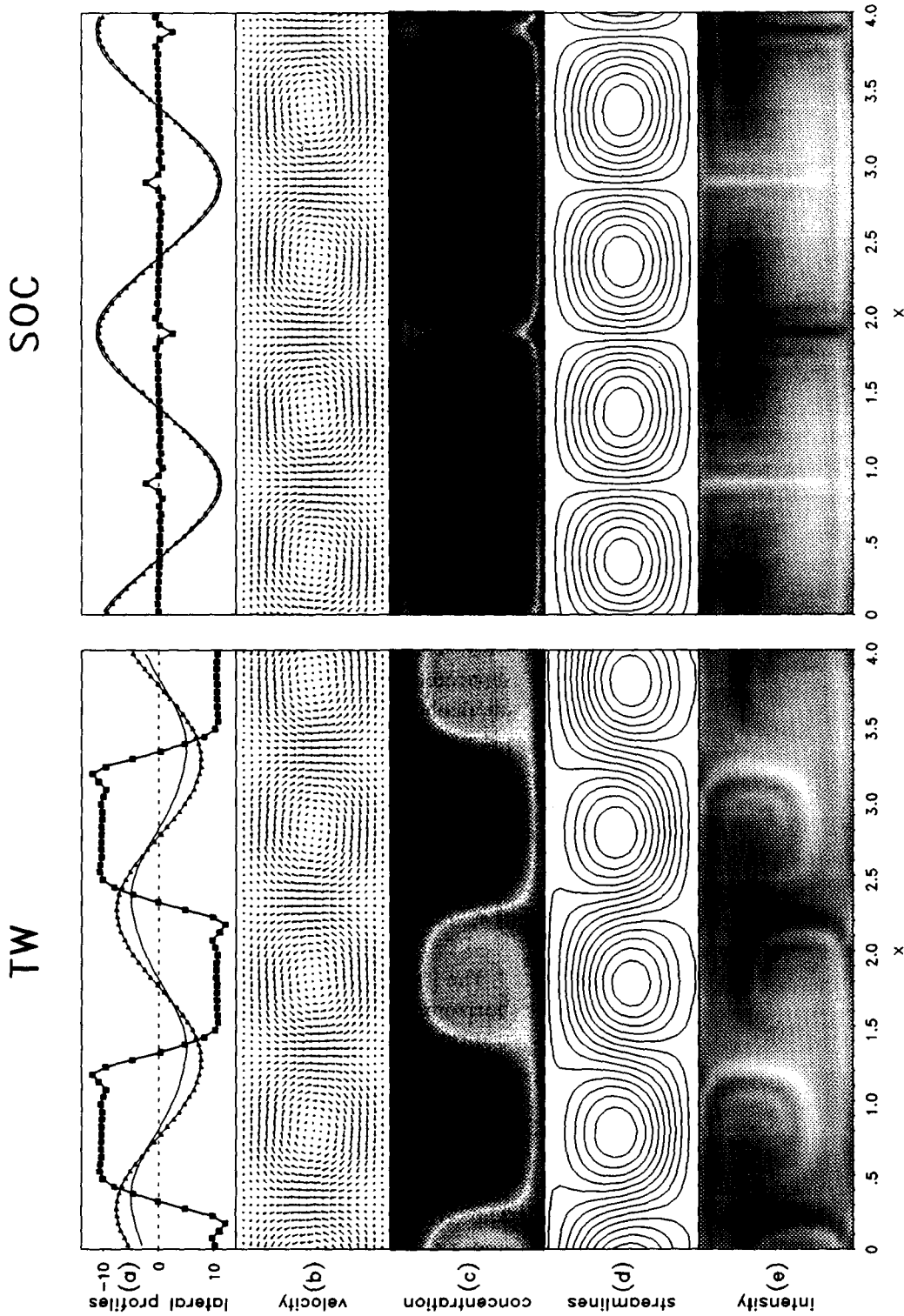


Fig. 2. Representative extended states from fig. 1: right propagating TW (left plate) with $\omega = 0.3\omega_H$ at $r = 1.216$, i.e., close to the saddle $r_{TW}^* \approx 1.215$ and SOC state (right plate) at $r = 1.823$ above $r^* \approx 1.65$. (a) Lateral profiles at midheight, $z = 1/2$, of w (thin line), $40 \delta T$ (triangles), and $400 \delta C$ (squares). (b) Velocity field. (c) Concentration field. For the TW blue at the top (red at the bottom) represents $\delta C \approx 0.05$ (-0.05) in units of $\Delta T \alpha / \beta$. For the SOC the vertical concentration contrast is smaller. There blue (red) represents $\delta C \approx 0.03$ (-0.03). In each case green denotes the mean concentration C_0 . (d) Velocity streamlines – for the TW in the frame comoving with the phase velocity to the right. (e) Intensity distribution $I(x, z)$ (3.1) of side view shadowgraph pictures. Vertical stripes in (c) and (e) are artefacts of the printer.

the top and bottom plates and between the rolls increase. The lateral TW concentration profile at $z = \frac{1}{2}$ (fig. a of the left plate) shows a characteristic, anharmonic, trapezoidal shape with linear pieces between the different concentration plateaus of adjacent rolls. With increasing r and decreasing TW frequency the plateau heights decrease and only the spikes between the rolls remain becoming more and more mirror symmetric. This mirror symmetry restoring development has been seen also experimentally in *top view* shadowgraph intensity profiles [7] that agree very well with our numerical results [7].

The *side view* shadowgraph intensity distributions shown in fig. 2e reflect to a large extent the structure of the concentration fields in fig. 2c which explains why this experimental technique can be used to extract [8] quantitative information on the concentration field structure in TW states. The influence of the concentration field on top view shadowgraph intensity profiles has first been elucidated by Eaton et al. [7] by comparing experimental and our numerical top view profiles.

3.3. Passive scalar motion and the TW concentration contrast

We now explain why in a right propagating TW the right (left) turning roll is alcohol rich (poor). To that end we observe this state from the frame of reference Σ' comoving with the phase velocity $v_p = \omega/k$ of the TW. In that frame the streamlines (shown in 2d) are the path lines of passively advected particles. Their structure can easily be understood [48,24,31,36] to follow from a stream function that has the form

$$\phi(x', z) = -\frac{1}{k} \tilde{w}(z) \sin(kx') - v_p z \quad (3.3)$$

if one approximates the vertical velocity field by $w \approx \tilde{w}(z) \cos[k(x - v_p t)]$. The contribution $v_p z$ has two effects: it shifts the closed equipotential lines alternately towards the top and bottom plates and furthermore it generates open stream-

lines meandering between and around the roll like regions. As an aside we mention that passive particles trapped on some [31] of the latter also show a large-scale backwards motion in the laboratory frame [24,31,36]. Note however, that this complicated *Lagrangian* particle motion which is a trivial consequence of any velocity potential like (3.3) should not be confused with the large-scale currents discussed in section 3.4.

On the other hand, the alternately upwards and downwards shifted roll regions together with the open stream lines separating them in the frame Σ' suggest a simple mechanism to explain the two different concentration levels of the TW: In fig. 2d there are vertical jets near the plates at $x \approx 0.2, 2.2$ ($x \approx 1.2, 3.2$) that transport alcohol poor (rich) fluid marked in red (blue) in fig. 2c upwards (downwards) from the bottom (top) plate where the Soret effect has depleted (enriched) the alcohol content. These red (blue) jets inject alcohol poor (rich) fluid from the bottom (top) boundary layer into the left (right) turning rolls. There the fluid is then mixed in each roll separately with the open streamlines prohibiting an alcohol exchange between the rolls. This simple explanation works because the concentration dynamics is dominated by advection with the diffusive contribution being small ($L \ll 1$) except in boundary layers which have large gradients.

3.4. Phase induced lateral currents

The TW state supports global, stationary, horizontal mean convective currents of concentration and heat:

$$\langle J_x \rangle = \langle u \delta C \rangle, \quad (3.4a)$$

$$\langle Q_x \rangle = \langle u \delta T \rangle. \quad (3.4b)$$

The concentration current $\langle J_x \rangle$ flows in the upper (lower) half of the fluid layer into (opposite to) the propagation direction of the TW and the heat current $\langle Q_x \rangle$ is directed opposite to

$\langle J_x \rangle$ ^{#4}. Here we average over a TW period in space or time. The currents (3.4) having mirror symmetric profiles [34] around midheight integrate vertically over the whole height of the layer to zero. Their size increases roughly linearly with the TW frequency [36].

The currents are driven [30,31] by the phase difference between the vertical velocity field and the concentration or temperature field, respectively: one finds [36] that the mean currents

$$\langle u \delta F \rangle \approx \frac{-1}{2k} |\hat{f}_1(z)| |\partial_z \hat{w}_1(z)| \sin(\varphi_t - \varphi_w) \quad (3.5)$$

are well approximated by a product of the first lateral Fourier mode of the concentration or temperature field, $\hat{f}_1(z)$, and that of u . The argument of the sine in (3.5) is the phase difference between the first lateral modes of F and w where $\delta F = \text{Re} \sum_n \hat{f}_n(z) e^{inkx}$ and $\hat{f}_n = |\hat{f}_n| e^{-i\varphi_n}$. In fig. 2a one sees that the temperature wave slightly lags behind the w -wave while the concentration wave is about $\frac{1}{2}\pi$ ahead of the w -wave. The latter phase relation reflects the fact that in the center of right (left) turning blue (yellow) rolls where $w = 0$ the concentration δC has a large positive (negative) value for the reasons described in the previous section.

One should not try to explain the mean lateral currents $\langle u \delta F \rangle$ (3.4) by moving a snapshot of the field δF , like that one in fig. 2c for δC as a whole with the TW phase velocity v_p . That procedure would generate a current $v_p \langle \delta F \rangle$ irrespective of the phase relation of δF and u . Furthermore, its vertical profile would be that of the zeroth lateral Fourier mode of δF . The mean concentration current does not arise because the concentration pattern of fig. 2c propagates but because velocity and concentration fields are phase shifted – even stationary fields would generate a mean convective current (3.5) if they were phase shifted.

^{#4}In refs. [34, 36] the directions of the currents are erroneously described as being opposite to the correct ones. The correct profiles are shown in fig. 5b of ref. [34].

For the extended TW states with spatial periodicity as, e.g., in annular experimental cells the physical significance of the above currents is not clear. However, in spatially confined LTW convection the large-scale concentration current plays a very important role (cf. below).

4. Spatially confined states: localized traveling convective rolls

In this section we discuss LTW states at $\psi = -0.25$ and at $\psi = -0.08$. At $\psi = -0.25$ LTW's with various widths have been seen in experiments in annular cells [10,15] and in our simulation [40] as stable states while at $\psi = -0.08$ only LTW's with uniquely selected width have been seen in experiments [11,12,14,16] and simulation [40]. Here we present a comparison between a representative example of each variety to show common features and differences.

4.1. Bifurcation diagrams

Fig. 3 shows the LTW states discussed here by open circles in the bifurcation diagrams of frequency and vertical convective flow amplitude, w_{\max} , versus Rayleigh number. For orientation the extended TW and SOC states are included by full symbols. The TW states of fig. 3 for $\psi = -0.25$ are also shown in fig. 1. The LTW flow amplitudes are only slightly smaller but the LTW frequencies are considerably larger than those in the competing extended states at the same r . In fact, for $\psi = -0.08$ the extended SOC state has zero frequency. On the other hand, ω_{LTW} is in each case considerably smaller than the frequency of small-amplitude linear perturbations of the conductive state at this r .

For $\psi = -0.25$, $r = 1.246$ we have evaluated LTW's having widths $l = 6.5$ and 8.9 in a $\Gamma = 20$ system. The latter state increased its width to $l = 9.9$ in a $\Gamma = 40$ system. All these states have very similar ω and w_{\max} . The structure of the fields under the fronts of the LTW regions is the

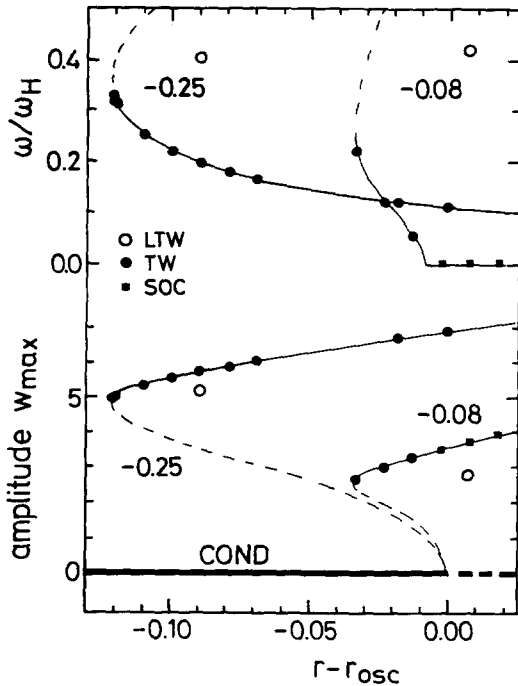


Fig. 3. LTW states (open circles) discussed here in the bifurcation diagrams of frequency ω and of maximal vertical flow velocity w_{\max} vs. Rayleigh number for $\psi = -0.25$, -0.08 . Full symbols are numerically obtained extended states. Thin lines are hand drawn guides to the eye. Schematic dashed ones for unstable lower branches show the bifurcation topology of TW's [38] and SOC's [30]. For $\psi = -0.25$, -0.08 the oscillatory threshold is at $r_{\text{osc}} = 1.3347$, 1.0965 [45]; Hopf frequency $\omega_H = 11.235$, 5.753 [45]; group velocity of linear TW at onset $v_g^c = \omega_H/\pi$ [44]; TW saddle $r_{\text{TW}}^s \approx 1.215$, 1.06 [36]; transition TW \leftrightarrow SOC $r^* \approx 1.65$, 1.09 [36]. Our LTW's are at $r - r_{\text{osc}} = -0.089$, 0.008 .

same – only the extension of the center part of these states differ. However, despite applying various numerical procedures for $\psi = -0.08$, $r = 1.104$ we found there only one LTW with the uniquely selected width $l \approx 4.9$ that agrees with experimental results [11,16].

The LTW at $\psi = -0.08$ is supercritical, i.e., stable above the convective onset r_{osc} . Thus, spatially confined convection stably coexists here with quiescent conduction in the remainder of the system despite the fact that the latter state is unstable. To explain this feature it has been suggested [40,13] and experimentally seen [12] and analyzed [17] that small-amplitude perturbations growing out of the unstable conductive

region are swept convectively with the fast group velocity of linear TW's into the large-amplitude nonlinear pulse-like LTW region in laterally periodic systems. See refs. [17,14] for further discussions. However, the absorption of small-amplitude perturbations by the pulse does not explain its very existence with a fixed extension, i.e., the fact that the nonlinear TW does not expand into an extended state which is stable at the same Rayleigh number.

4.2. LTW's of arbitrary and selected width: a comparison

Fig. 4 shows some structural properties of LTW states obtained in our simulation. Their

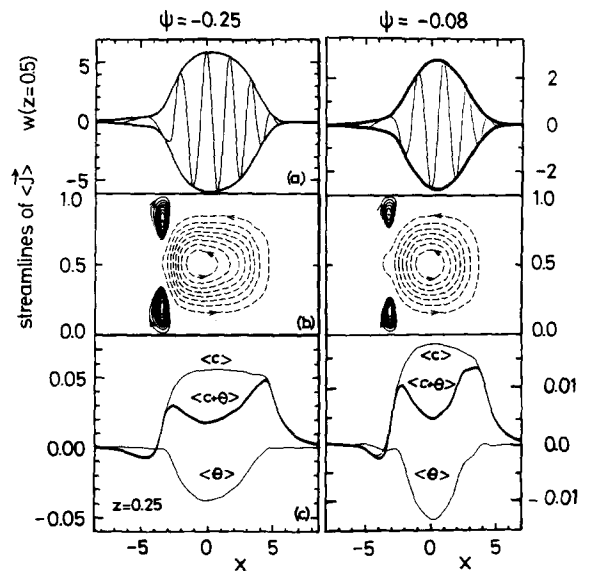


Fig. 4. Lateral structure of the LTW states shown in fig. 3 by open circles. Phase and group velocities of both states are to the left. (a) Snapshot of the vertical velocity field at midheight (thin lines) and its envelope (thick lines) below which the wave train moves during one oscillation period. (b) Streamlines of the mean concentration current $\langle \mathbf{J} \rangle$ (4.3) are shown by dashed (full) lines for the large-scale, large-amplitude primary (small-amplitude secondary) current loops. For better presentation the stream-function scale has been magnified for the full lines. (c) Lateral profiles of $\langle c \rangle$ and $\langle \theta \rangle$ are shown at $z = 0.25$ together with $\langle c + \theta \rangle$ determining the convective contribution to the mean buoyancy force. The states shown are characterized for $\psi = -0.25$, -0.08 by $r = 1.246$, 1.104 ; $\omega = 4.51$, 2.42 ; $v_g = 0.054$, 0.052 ; width 6.5 , 4.9 .

location in the bifurcation diagrams of fig. 3 is marked by the open circles. In both states the phase velocity as well as the group velocity v_g of the envelope is to the left. However, v_g is by a factor of ≈ 30 for $\psi = -0.25$ (15 for $\psi = -0.08$) smaller than the mean phase velocity of the LTW. Furthermore v_g is smaller than the group velocity v_g^c of linear TW's at onset [44] by a factor of ≈ 70 for $\psi = -0.25$ (35 for $\psi = -0.08$). For $\psi = -0.25$ v_g slightly decreases with increasing width.

The LTW states are time periodic with period τ in the reference frame $\tilde{\Sigma}$ that comoves with the group velocity

$$\tilde{F}_{\text{LTW}}(\tilde{x}, z; t) = \tilde{F}_{\text{LTW}}(\tilde{x}, z; t + \tau). \quad (4.1a)$$

Furthermore the fields display in this frame the symmetry

$$\delta \tilde{F}_{\text{LTW}}(\tilde{x}, z; t) = \pm \delta \tilde{F}_{\text{LTW}}(\tilde{x}, 1 - z; t + \frac{1}{2}\tau) \quad (4.1b)$$

under time translation by $\frac{1}{2}\tau$ combined with vertical reflection at the mid-layer plane $z = \frac{1}{2}$. The extended TW shows the symmetries (4.1) in the laboratory frame and, in addition, the symmetry (3.2) that is broken by the lateral intensity variation of the LTW.

In the center part of the LTW's, in particular in those of larger extension, the fields are very similar to those we would expect for an extended TW with similar frequency. Hence, since the concentration field shows the strongly anharmonic variation discussed for TW's in section 3.2, LTW's are strongly nonlinear states with a lateral spatial structure differing substantially from that of the critical wave, $e^{ik_c x}$. Furthermore, the envelope of the fields of w , θ , and c all differ in shape and extension so that also for this reason the LTW is not just a wave packet, $\sim A(x) e^{ik_c x}$, of harmonic waves with a common envelope $A(x)$.

Comparing the LTW's of different widths at $\psi = -0.25$ with the one at $\psi = -0.08$ with select-

ed width one finds that they basically differ only in the extension of their center part: Not only do the streamlines of the mean concentration current $\langle J \rangle$ in fig. 4b reveal the same concentration transport mechanism (discussed further below) but, more importantly, the envelope and structure of all fields in the leading edge of each LTW state is practically the same for the different states as well as the envelope and field structure in the trailing edge. This holds for w shown in fig. 4a but also for θ and c . The local wavelength $\lambda(x)$ drops in both LTW states monotonously from $\lambda \approx 2$ under the leading edge to a value of $\lambda \approx 1.5$ under the trailing edge with some $\lambda < \lambda_c$ in the center portion. The spatial variation of $\lambda(x)$ under the respective edges is the same for both states whereas with a growing center extension in a wider LTW state a plateau like part of $\lambda(x)$ opens up. The characteristic variation of $\lambda(x)$ obtained in the simulation [40] has been found also in experiments for $\psi = -0.25$ [15] and $\psi = -0.123$ [16]. To sum up: the wider LTW states have the same front structure as the narrow uniquely selected LTW state at $\psi = -0.08$ which just lacks a sizeable center part. While this observation does not explain the appearance of an arbitrary (uniquely selected) width at $\psi = -0.25$ (-0.08) it might help in finding an explanation.

We finally mention that the envelopes of the w , θ , and c fields are to a varying degree asymmetric [40] around the respective center. Furthermore, they have also different extensions. In particular the localized concentration wave is significantly wider than the localized velocity wave. Common to them, however, is that the leading fronts are steeper than the trailing ones and that the field amplitudes are largest just behind the leading front. On the other hand, the top view shadowgraph intensity distribution

$$I(x) = \int_0^1 dz \partial_x^2 (C + aT) \quad (4.2)$$

is more symmetric [15] since the second deriva-

tive in (4.2) depresses (enhances) the leading (trailing) parts of the LTW's with the small (large) local wave numbers. The experimentally observed shadowgraph intensity variation at $\psi = -0.25$ is in good agreement [15] with (4.2) obtained from the simulation.

4.3. Large-scale current and concentration redistribution

We discuss here the effect of a large-scale current-induced concentration redistribution [40] upon the pulse velocity. Such a redistribution has earlier been speculated upon [31,32]. This effect being outside the range of a one-mode, single-field amplitude equation (cf. [46] for a first attempt to model it) seems to be able to explain the very small group velocities observed in our simulation. Recent experiments [16,20] in very homogeneous cells also showed very small Rayleigh number dependent drift velocities that are only slightly smaller than our results.

The phase shift between vertical velocity and concentration waves in the center part of the LTW state drives there as in the extended TW a strong large-scale mean concentration current

$$\langle \mathbf{J} \rangle = \langle \delta C \mathbf{u} \rangle - L \nabla \langle C - \psi T \rangle \quad (4.3)$$

that flows in the upper (lower) half of the layer parallel (antiparallel) to the phase velocity. Since in the quiescent conductive state there can be no concentration current the latter is deflected vertically under the fronts of the LTW to form a large primary concentration circulation loop shown by dashed lines in fig. 4b. Under the leading (trailing) front the vertical current $\langle J_z \rangle$ is laterally focused (dilated). Since part of $\langle J_z \rangle$ is diffusive under the fronts and since the θ pulse is narrower than the c pulse (cf. fig. 4c) the associated mean vertical concentration gradient around midheight of the layer is bigger (smaller) under the leading (trailing) front than in the conductive state. So the current sustains relative to the conductive concentration stratification a small

concentration surplus (deficiency) in the upper (lower) half of the layer just ahead of the leading front – cf. fig. 3a in ref. [40]. In this transition region from conduction to convection the above concentration difference generates at the plates a diffusive lateral current $-L \partial_x \langle c \rangle$. While it strengthens at the trailing front the large primary concentration loop it is directed under the leading front opposite to the primary current, thus generating two small secondary counter circulating current loops (full lines in fig. 4b) under the leading front of the pulse.

Thus the net overall effect of the primary lateral current that is generated in the center part of the pulse and that transports concentration to (away from) the leading front is to deposit (withdraw) concentration in the region ahead of the leading front in the upper (lower) half of the layer. The resulting concentration barrier ahead of the leading front stabilizes the conductive state and hinders convection since the convective contribution

$$\langle b - b_{\text{cond}} \rangle = \sigma R \langle c + \theta \rangle \quad (4.4)$$

reduces the size of the mean buoyancy force. Simultaneously convection is strengthened at the trailing edge against invasion of the conductive state. The negative dip in the thick full line in fig. 4c showing $\langle c + \theta \rangle$ at $z = \frac{1}{4}$ demonstrates the vertically downwards, i.e., stabilizing contribution from $\langle c \rangle$ to $\langle b \rangle$ in the lower half of the layer. Similarly in the upper half $\langle c + \theta \rangle$ is positive there so that again the convective contribution is stabilizing, i.e., upwards. In the center of the pulse the convective part (4.4) enhances the driving force.

We believe that this interplay between the structural dynamics of a confined pattern, the large-scale current generated by the latter, and the resulting large-scale field modification explains why the drift velocity is reduced so dramatically from v_g^c to almost zero. Furthermore, from the results obtained for TW's one infers that the strength of the current and the

resulting concentration redistribution which hinders convection at the leading pulse front increase with growing frequency, i.e., decreasing Rayleigh number. Thus the drift velocity decreases upon reducing r as found experimentally [16,20]. Also drift velocities opposite to the phase velocity at the smallest Rayleigh numbers [20] can be explained when the current-induced concentration redistribution becomes strong enough to “overstabilize” (enhance) the conductive (convective) state ahead of (behind) the pulse so that the conductive state no longer recedes at the leading front from the pulse but expands thereby pushing the pulse backwards, i.e., opposite to its phase velocity. Finally an explanation of the collision behaviour [25] of two pulses seems to be feasible with the large-scale current induced concentration redistributions that affect the buoyancy forces at the pulse fronts.

5. Concluding remarks

The importance of the role that the concentration field plays in the convective states of binary mixtures discussed here can easily be appreciated by comparing these states with convection in the corresponding pure fluid, $\psi = 0$, at the same Rayleigh and Prandtl number. Thus one sees that the appearance of an oscillatory convective instability, the backwards hysteretic bifurcation topology for negative ψ , the existence of TW convection and of LTW states are all consequences of the concentration field being coupled via the Soret effect to the temperature: The Soret coupling with the degrees of freedom represented by the concentration field generates in the linear dynamics of perturbations around the conductive state an effective “restoring force” in the language of mechanical systems for the perturbations. The appearance of the associated pair of complex conjugate characteristic exponents resulting at negative ψ for any Lewis number (not just $L \ll 1$) from the “off-diagonal”

Soret coupling can be understood most easily with one-mode representations for each field. Then, having perturbations at threshold of the form $e^{i\omega t} e^{ikx}$ the possibility of TW states is obvious. Furthermore, the suppression of the buoyancy for $\psi < 0$ by the Soret induced concentration distribution together with the nonlinear feedback resulting from the buoyancy enhancement by convective homogenization makes the transition first order, i.e., causes hysteretic backwards bifurcation branches. Finally, complex Ginzburg–Landau equations with quintic amplitude terms that capture the subcritical nature of the bifurcation TW branch suggest the existence of spatially confined convective regions embedded below the convective threshold in the stable conductive state. However, the structure and dynamics of these nonlinear LTW states are very strongly influenced by the concentration field.

Acknowledgements

Discussions with G. Ahlers, K.D. Eaton, P. Kolodner, D.R. Ohlsen, and C.M. Surko are gratefully acknowledged. This work was supported by Deutsche Forschungsgemeinschaft.

References

- [1] J.K. Platten and J.C. Legros, *Convection in Liquids* (Springer, Berlin, 1984).
- [2] R.W. Walden, P. Kolodner, A. Passner, and C.M. Surko, *Phys. Rev. Lett.* 55 (1985) 496.
- [3] E. Moses and V. Steinberg, *Phys. Rev. A* 34 (1986) 693.
- [4] R. Heinrichs, G. Ahlers and D.S. Cannell, *Phys. Rev. A* 35 (1987) 2761.
- [5] O. Lhost and J.K. Platten, *Phys. Rev. A* 38 (1988) 3147; *A* 40, (1989) 4552.
- [6] D.R. Ohlsen, S.Y. Yamamoto, C.M. Surko and P. Kolodner, *Phys. Rev. Lett.* 65 (1990) 1421.
- [7] K.D. Eaton, D.R. Ohlsen, S.Y. Yamamoto, C.M. Surko, W. Barten, M. Lücke, M. Kamps and P. Kolodner, *Phys. Rev. A* 43 (1991) 7105.
- [8] B.L. Winkler and P. Kolodner, *J. Fluid Mech.* 240 (1992) 31.

- [9] E. Moses, J. Fineberg and V. Steinberg, *Phys. Rev. A* 35 (1987) 2757.
- [10] P. Kolodner, D. Bensimon and C.M. Surko, *Phys. Rev. Lett.* 60 (1988) 1723;
D. Bensimon, P. Kolodner, C.M. Surko, H. Williams and V. Croquette, *J. Fluid Mech.* 217 (1990) 441.
- [11] J.J. Niemela, G. Ahlers and D.S. Cannell, *Phys. Rev. Lett.* 64 (1990) 1365.
- [12] K.E. Anderson and R.P. Behringer, *Phys. Lett. A* 145 (1990) 323; *Physica D* 51 (1991) 444.
- [13] G. Ahlers, private communication.
- [14] V. Steinberg and E. Kaplan, in: *Spontaneous formation of space-time structures and criticality*, eds. T. Riste and D. Sherrington, NATO ASI Series (Plenum), to appear.
- [15] C.M. Surko, D.R. Ohlsen, S.Y. Yamamoto and P. Kolodner, *Phys. Rev. A* 43 (1991) 7101.
- [16] P. Kolodner, *Phys. Rev. A* 44 (1991) 6448.
- [17] P. Kolodner and J. Glazier, *Phys. Rev. A* 42 (1990) 7504;
J. Glazier and P. Kolodner, *Phys. Rev. A* 43 (1991) 4269.
- [18] G. Ahlers, *Physica D* 51 (1991) 421.
- [19] T. Katoh and Y. Sawada, *J. Phys. Soc. Japan* 58 (1989) 3879.
- [20] P. Kolodner, *Phys. Rev. Lett.* 66 (1991) 1165.
- [21] T.S. Sullivan and G. Ahlers, *Phys. Rev. Lett.* 61 (1988) 78.
- [22] V. Steinberg, J. Fineberg, E. Moses and I. Rehberg, *Physica D* 37 (1989) 359.
J. Fineberg, E. Moses and V. Steinberg, *Phys. Rev. A* 38 (1988) 4939.
- [23] S. Rasenat, G. Hartung, B.L. Winkler and I. Rehberg, *Experiments in Fluids* 7 (1989) 412.
- [24] E. Moses and V. Steinberg, *Phys. Rev. Lett.* 60 (1988) 2030; *Physica D* 37 (1989) 341.
- [25] P. Kolodner, *Phys. Rev. A* 44 (1991) 6466.
- [26] P. Kolodner and C.M. Surko, *Phys. Rev. Lett.* 61 (1988) 842;
C.M. Surko, P. Kolodner, A. Passner and R.W. Walden, *Physica D* 23 (1986) 220.
- [27] P. Kolodner, H. Williams and C. Moe, *J. Chem. Phys.* 88 (1988) 6512.
- [28] E. Knobloch, *Phys. Rev. A* 34 (1986) 1538.
- [29] W. Schöpf and W. Zimmermann, *Europhys. Lett.* 8 (1989) 41.
- [30] S.J. Linz and M. Lücke, *Phys. Rev. A* 35 (1987) 3997;
in: *Propagation in Systems Far from Equilibrium*, eds. J.E. Wesfreid, H.R. Brand, P. Manneville, G. Albinet and N. Boccara (Springer, Berlin, 1988) p. 292.
- [31] S.J. Linz, M. Lücke, H.W. Müller and J. Niederländer, *Phys. Rev. A* 38 (1988) 5727.
- [32] M. Lücke, in: *Far from Equilibrium Phase Transitions*, *Lecture Notes in Physics*, Vol. 319, ed. L. Garrido (Springer, Berlin, 1988) p. 195.
- [33] A.E. Deane, E. Knobloch and J. Toomre, *Phys. Rev. A* 37 (1988) 1817.
- [34] W. Barten, M. Lücke, W. Hort and M. Kamps, *Phys. Rev. Lett.* 63 (1989) 376.
- [35] H. Yahata, *Prog. Theor. Phys. Suppl.* 99 (1989) 4939.
- [36] W. Barten, M. Lücke and M. Kamps, in: *Nonlinear Evolution of Spatio-Temporal Structures in Dissipative Continuous Systems*, NATO ASI Series B2. 225, eds. F. Busse and L. Kramer (Plenum Press, 1990) p. 131.
- [37] H. Yahata, *Prog. Theor. Phys.* 85 (1991) 933.
- [38] D. Bensimon, A. Pumir and B.I. Shraiman, *J. Phys. (Paris)* 50 (1989) 3089.
- [39] M.C. Cross, *Phys. Rev. Lett.* 57 (1986) 2935; *Phys. Rev. A* 38 (1988) 3593.
- [40] W. Barten, M. Lücke and M. Kamps, *Phys. Rev. Lett.* 66 (1991) 2621.
- [41] O. Thual and S. Fauve, *J. Phys. (Paris)* 49 (1988) 1829; *Phys. Rev. Lett.* 64 (1990) 282.
- [42] W. van Saarloos and P.C. Hohenberg, *Phys. Rev. Lett.* 64 (1990) 749.
- [43] H.R. Brand and R.J. Deissler, *Phys. Rev. Lett.* 63 (1989) 2801;
R.J. Deissler and H.R. Brand, *Phys. Lett. A* 146 (1990) 252.
- [44] E. Knobloch and D.R. Moore, *Phys. Rev. A* 37 (1988) 860;
M.C. Cross and K. Kim, *Phys. Rev. A* 37 (1988) 3909; *A* 38 (1988) 529.
- [45] W. Hort, Diplomarbeit, Universität Saarbrücken, 1990, unpublished.
- [46] H. Riecke, *Phys. Rev. Lett.* 68 (1992) 301.
- [47] G. Veronis, *J. Mar. Research* 23 (1965) 1.
- [48] E. Knobloch and J.B. Weiss, *Phys. Rev. A* 36 (1987) 1522.
- [49] S.J. Linz, Ph.D. thesis, Universität Saarbrücken, 1989, unpublished.
- [50] H.R. Brand, P.C. Hohenberg and V. Steinberg, *Phys. Rev. A* 30 (1984) 2548;
H.R. Brand, P.S. Lomdahl and A.C. Newell, *Physica D* 23 (1986) 345.
- [51] M. Bestehorn, R. Friedrichs and H. Haken, *Z. Phys. B* 75 (1989) 265.
- [52] O. Lhost, S.J. Linz and H.W. Müller, *J. Phys. II* 1 (1991) 279.
- [53] J.E. Welch, F.H. Harlow, J.P. Shannon and B.J. Daly, Los Alamos Scientific Laboratory Report No. LA-3425, 1966.
- [54] C.W. Hirt, B.D. Nichols and N.C. Romero, Los Alamos Scientific Laboratory Report No. LA-5652, 1975.
- [55] W. Barten, M. Lücke and M. Kamps, *J. Comput. Phys.* 91 (1990) 486.